HYDRODYNAMIC MODELLING OF LASER PLASMA IONIZATION PROCESSES

A. VERTES * and P. JUHASZ

Central Research Institute for Physics, Hungarian Academy of Sciences, P.O. Box 49, H-1525 Budapest 114 (Hungary)

M. DE WOLF and R. GIJBELS

University of Antwerp (U.I.A.), Department of Chemistry, Universiteitsplein 1, B-2610 Wilrijk (Belgium)

ABSTRACT

A one-component one-dimensional (1C 1D) hydrodynamic model has been developed to describe the expansion of laser-generated plumes in ion sources. The model incorporates the conservation formalism of hydrodynamics, normal and plasma absorption mechanisms of laser–target coupling and the local thermal equilibrium condition for ionization. The considerable difficulties (non-linearities, shock waves) in finding the solution were overcome by using the Godunov algorithm.

A comprehensive study of the model covered three different laser types (ruby, CO_2 and frequency-quadrupled Nd–YAG) and three classes of solid targets (metals, transparent insulators and opaque insulators). Density, velocity and temperature profiles across the expanding plume were evaluated at the end of the laser pulse, to yield crater depths, cloud extensions, ion yields, relative sensitivity factors and ion kinetic energy distributions, i.e. quantities more closely related to experimental data.

Although calculated crater depths significantly exceeded the measured values, they show strong correlation with them. We found that the extension of the gas cloud varied with the laser power density according to a power law. A similar conclusion can be drawn from expansion velocity measurements (even providing exponents that are close in value).

Calculated ion yield versus laser intensity curves show the typical threshold behaviour separating laser desorption and laser plasma ionization. In the plasma ionization mode the known uniform relative sensitivity factors were recovered.

Ion kinetic energy distributions were investigated under typical laser desorption and laser plasma ionization conditions. The energy spectrum of the desorbed ions extended up to 1 eV, in good agreement with measured spectra. Laser plasma ionization provided ions with up to 100 eV, therefore somewhat underestimating experimental values.

---

* Author to whom correspondence should be addressed. Present address: University of Antwerp (U.I.A.), Department of Chemistry, Universiteitsplein 1, B-2610 Wilrijk, Belgium. Electronic mail: VERTES@BANUIA 52. BITNET.

INTRODUCTION

Laser ionization is increasingly recognized as a flexible and effective method of ion production for mass spectrometric analysis. It can produce ions characteristic of non-volatile organic solids and of insulating inorganic materials with virtually no sample preparation. Changing the intensity of the laser pulse allows one to choose between the mild laser desorption mode where quasi-molecular ions are created and the laser plasma ionization mode where elemental ions are abundant.

In recent years laser desorption mass spectrometry (LDMS) has become one of the most fruitful branches of mass spectrometry, especially for analysing non-volatile organic compounds. Apart from the accumulated experimental experience, which has been compiled in several places [1,2], it has also found theoretical footing for the ion formation mechanisms which may range from resonant photoionization to ion neutral attachment reactions [3,4]. In spite of quite diverse theoretical efforts, however, there are many unclear points in the understanding of the formation of mass spectra, among them the unexpectedly high kinetic energy of the laser-generated ions [5].

Laser plasma ionization mass spectrometry (LPIMS), which operates in the higher power density domain (over 10^8 W cm^{-2}), has also gained considerable importance during the 1970s and 1980s as a trace analytical method for elements. The present understanding of atomization and ion formation mechanisms involved in LPIMS is based on the assumption of a hot transient plasma in front of the sample, created and heated by the laser pulse.

The origin of ions generated in the laser target interaction has been widely discussed in the literature [1]. According to the prevailing judgement, the different targets, lasers and irradiances give rise to different mechanisms. In a rough classification, thermal and non-thermal processes are distinguished. The latter include photo-ionization on the surface and in the gas phase, Coulomb explosion and surface-assisted ionization.

In this study we have tried to outline and resolve a possible mechanism of ion formation and plasma generation based entirely on thermal processes. In doing so, we did not want to exclude other possibilities or their combinations with the mechanism discussed here. Rather, we tried to appraise the contribution of some thermal and plasma processes to laser ionization.

In a recent review [6] we made an attempt to describe laser ionization processes in terms of energy deposition, a concept that has found wide application in the theory of secondary ion mass spectrometry (SIMS) [7]. In the present work we wish to extend the investigations described in [6] to pursue a systematic study of laser ionization processes in the following

respects: effect of the laser wavelength; effect of the optical properties of the sample; kinetic energy distribution of ions; and reason for elemental sensitivity factors being so uniform.

According to a crude classification, we can specify three basically different levels for describing the laser–target interaction.

In the simplest case, we neglect all interactions between the individual particles and assume that they are subjected exclusively to external fields. In this case, ions and neutrals would be exposed to the laser field and the external accelerating field. However, it is clear from a large number of experiments that collective motion and ion–neutral collisions have a profound influence on the laser ionization mass spectra [8,9].

The other extreme of the description levels is the kinetic theoretical approach. It is well known that we cannot rely on equilibrium thermodynamics in the case of laser ionization, because the processes underlying the interaction of a solid sample with short laser pulses are of highly non-equilibrium character. However, the kinetic approach based on the approximate solution of the Boltzmann equation has enormous computational difficulties and also contains experimentally unavailable quantities (i.e. we are not able to measure the position- and time-dependent velocity distribution function). Although Sigmund's results, which were derived from a kinetic theoretical description, are successful in SIMS [10], the enormous difference in the number of elementary events makes this approach unsuitable for laser ionization.

Between the two extreme cases we find a useful compromise: the hydrodynamic approach. Its advantages are the following: hydrodynamics provides us with the ion density, velocity and temperature profiles in the ion source and leads to quantities which are readily measurable. For example, ion yields, crater depth in the target, estimates for the relative sensitivity factors (RSF), and the kinetic energy distribution of the ions can be determined from the profiles mentioned above. Furthermore, in the case of laser ionization processes from a bulk sample it is demonstrated that a significant part of the ionizing beam's energy is converted into hydrodynamic flow [6,11].

Although detailed hydrodynamic calculations have not been applied up to now to investigate phenomena occurring in laser mass spectrometric ion sources, similar calculations have been carried out in the early 1970s in the field of laser fusion research [12,13]. Since then, numerous computational codes have been published for the simulation of laser–plasma interaction, using Monte Carlo simulations and three-dimensional hydrodynamic calculations [14]. Our specific needs were different as, because of lower laser power densities in LIMS, the underlying physical processes and, consequently, the models were different. Our aim was to study the behaviour of

the laser-exposed target in conditions characterized by several parameters of the laser and of the target as well.

To carry out the necessarily lengthy calculations we decided to introduce a one-fluid one-dimensional model which also allowed several tests on the effect of microscopical details of laser–target interaction. In this paper we will sketch the technical details of our work very briefly. (A more detailed presentation is available to interested readers in the original paper of Godunov [15].) We will focus rather on the interpretation and discussion of the results, with emphasis on mass spectrometric applications.

In the following section, we outline our model for hydrodynamic motion in the ion source and for the laser absorption and ion formation in the target. Later, in the Results and Discussion section, we survey the predictions of the model for a few classes of materials; for example, metals, and transparent and opaque insulators. In addition, we investigate the effect of the laser wavelength and intensity, and other interesting implications, such as cloud extensions, kinetic energy distributions of ions, elemental sensitivity factors, and ion yields. We also discuss the question of the penetration of an electrostatic field into the laser-generated plasma.

METHODS OF CALCULATION

This section is subdivided into two parts: in the first we present the basic ingredients of hydrodynamics for our model, in the second we describe the laser heating of the system. The latter involves two absorption mechanisms to make distinction between thermal ionization and plasma ionization. The model of ion formation is formulated within the framework of the local thermal equilibrium (LTE) theory.

Hydrodynamics

In a previous paper [11] we described the physical situation at the very moment of the onset of the laser ionization process. From the solid–vacuum boundary, under vigorous heating by the laser, a rapid extension starts into the vacuum. We assume that this plasma expansion process is responsible for the physical and chemical properties of the generated ions. It is possible to describe these processes by hydrodynamics. Visualization of the laser–target interaction can be found in fig. 2 of [6].

Let us write down the system of equations of hydrodynamics in the conservative form and in a fixed external reference frame (i.e. the Eulerian description), in one dimension

$$\frac{\partial \mathbf{R}}{\partial t} = -\frac{\partial \mathbf{F}}{\partial x} \tag{1}$$

where the components of the generalized density vector, **R**, are the mass density, momentum density and energy density

$$R_1 = nm = \rho \qquad R_2 = \rho v \qquad R_3 = \rho \left(e + v^2/2 \right) \tag{2}$$

in terms of number density of the particles, n, mass of the particle, m, the hydrodynamic velocity, v, and the internal energy per unit mass, e. The generalized flux vector, **F**, has the following components:

$$F_1 = \rho v \qquad F_2 = p + \rho v^2 \qquad F_3 = \rho v \left(e + p/\rho + v^2/2 \right) - \Phi \tag{3}$$

where p denotes the pressure and Φ stands for the laser intensity. We see that Eq. 1 contains three separate equations and five unknown functions: ρ, v, e, p and Φ. To complete the system we accept the ideal gas law, which we write for a monoatomic gas

$$e = \tfrac{3}{2}(1 + \eta)kT + \eta U_i \tag{4}$$

where k is the Boltzmann constant, T is the absolute temperature, η is the degree of ionization and U_i is the ionization potential of the target material. The laser intensity is determined through an absorption law, which is treated in the next subsection together with the calculation of the degree of ionization.

The solid–vacuum boundary, before the laser pulse impinges on the target, represents a discontinuity in the initial conditions. The values of the hydrodynamic observables in the initial conditions differ by many orders of magnitude on the two sides of the solid–vacuum interface. In such cases these discontinuities evolve into hydrodynamic anomalies, i.e. shocks, rarefaction waves and contact discontinuities [16], in the course of the expansion. Such expansion processes may even be studied analytically [17], but only under serious limitations which include, among other, the absence of any external energy source such as, for instance, laser heating. The only tenable method to track laser-governed plasma expansion is the numerical solution of the equations of hydrodynamics.

The most important requirement for the method of solution was that these anomalies should be described in a physically consistent way. Further information on problems caused by shocks was given by Richtmyer and Morton [18]. The most widespread method for shock treating is the artificial viscosity method introduced by von Neumann and Richtmyer [19]; however, as was pointed out recently [20], this sometimes leads to unphysical solutions.

For that reason we have used another method, invented by Godunov et al. [21], which satisfies the main prerequisite mentioned above. Other properties of the method, such as stability and convergence, were also satisfactory. A detailed discussion of these numerical properties of the Godunov method can be found in ref. 18.

Godunov's scheme uses the following finite difference approximation of Eq. 1

$$\frac{\mathbf{R}_{j+1/2}^{n+1} - \mathbf{R}_{j+1/2}^{n}}{\Delta t} = \frac{\mathbf{F}_{j+1}^{n+1/2} - \mathbf{F}_{j}^{n+1/2}}{\Delta x} \tag{5}$$

In this equation the time levels are distinguished by superscripts, that is, $n + 1$ means $(n + 1)\,\Delta t$, and space points are labelled by subscripts, that is $j + 1$ means $(j + 1)\,\Delta x$.

Once the profiles of the generalized densities and fluxes are known at a certain time, we can determine them at the next time level by making use of Eq. 5, provided that it is possible to determine the flux profiles at the intermediate time level, $(n + 1/2)\,\Delta t$.

Godunov's idea was to utilize for this purpose analytically known breakdown formulae. It is known from hydrodynamics that the problem of breakdown of discontinuities can be solved analytically in certain circumstances [16]. The discretization of the profiles of the hydrodynamic variables can be seen as a juxtaposition of discontinuities which appear in the points of the spatial grid, on which the finite approximation has been made. Now the flux values at the intermediate time level have to be calculated through the analytically exact breakdown formulae for each discontinuity arising from the discretization of Eq. 1. The derivation of these formulae can be found in [15] and [18].

In the course of the calculations, real discontinuities of different kind may arise in the flow. For example because of the vigorous expansion of the material ablated by the laser a compression wave is generated and penetrates into the target. Another kind of discontinuity evolves in the gas phase where an intense pressure wave—called shock—emerges. As the Godunov method is based on the exact treatment of discontinuities, it is hoped that it will cope with real shocks and rarefaction waves.

Finally, it is important to stress that the breakdown formulae are derived for an ideal flow, which means, for instance, that no external or internal source of energy is allowed. Therefore, we had to tailor the method for our needs. The evolution of the system was considered as an alternating sequence of very short steps of expansion and light absorption.

Laser absorption and ion formation

Interaction of solids and plasmas with laser reveals a wide variety of processes even if we constrain ourselves to absorption. Therefore, simplification was inevitable. The minimal requirement was to make a proper distinction between laser desorption and plasma ionization. The competition between the two processes determines the features of the extracted mass spectra.

We have included two methods of absorption in our model: the first describes the absorption by the particles of the target and the second represents the plasma absorption. The importance of the former was emphasized earlier by Karas et al. [22,23], who studied the ion formation threshold for the laser intensity as a function of the absorption coefficient of the sample at the given laser wavelength. As for the plasma absorption, it has been proved that under the experimental conditions of mass spectrometry the so-called inverse Bremsstrahlung mechanism of the ionization is dominant [24,25].

In this picture the free electrons absorb photon(s) in the Coulomb-field of an ion or other electron and gain higher kinetic energy. The ionization takes place through collisions between atoms (molecules) and energetic free electrons. Other mechanisms of the ionization, such as, for example, multiphoton processes, were not considered here.

For the description of laser absorption we used a Lambert–Beer type formula

$$\Phi(x) = \Phi_0 \exp\left[-\int_{-\infty}^{x} \left[\alpha_0(x') + \alpha_{pl}(x') \right] \, dx' \right] \tag{6}$$

where the radiation intensity, Φ, is determined through the absorption coefficients α_0 and α_{pl}. As the absorbing medium was inhomogeneous, both absorption coefficients depended on the position. α_0 is a "normal" absorption coefficient which corresponds to transitions between discrete energy levels of internal degrees of freedom in the system. The position-dependence of this normal absorption coefficient, α_0, enters through the number density, $n(x)$ and the ionization degree, $\eta(x)$, profiles. In the case of normal absorption the dependence was a simple proportionality

$$\alpha_0 = \alpha_0' n(x)[1 - \eta(x)] \tag{7}$$

In this equation α_0' was determined by dividing the absorption coefficient of the material by the total number density of particles in the sample.

An expression for the plasma absorption coefficient, α_{pl}, can be found in [26]

$$\alpha_{pl}(n_e, T_e) = \frac{2\omega}{c} \, \text{Im} \sqrt{\left[1 - \frac{\omega_{pl}^2}{\omega^2\left(1 + \dfrac{i}{\tau_{ei}\omega}\right)} \right]} \tag{8}$$

where ω, c and τ_{ei} are the (angular) frequency of the laser, the velocity of light in vacuum, and the electron–ion collision time, respectively. $\omega_{pl} = (n_e e^2/4\pi m_e)^{1/2}$ is the electron plasma frequency, and e denotes the elec-

tronic charge. The most often used expression for the electron–ion collision time stems from Spitzer [27]

$$\tau_{ei}^{-1} = \frac{4\sqrt{(2\pi)}\,Z^2 e^4}{3\sqrt{(m_e)}\,k^{3/2}}\,\frac{n_i\,\ln\Lambda}{T_e^{3/2}}$$ (9)

where Z stands for the charge of ions, n_i for the ion density, T_e for the electron temperature and $\ln\Lambda$ for the Coulomb logarithm. This last factor is a delicate ingredient of the theory because it involves dynamical information about ion–electron collisions. According to Spitzer [27]

$$\Lambda = \frac{3}{2e_0^3}\left(\frac{k^3 T_e^3}{\pi n_e}\right)^{1/2}$$ (10)

A more detailed investigation of Eq. 8 reveals that the plasma absorption coefficient shows a pronounced maximum where the laser frequency is in the vicinity of the plasma frequency. If the free electron density is sufficiently close to the critical density, the plasma absorption coefficient will be higher than the normal absorption coefficient. We call this laser plasma ionization to distinguish it from the laser desorption (see ref. 41).

An important question we have to address is the validity of Eq. 6. It is well known that Eq. 6 is an exact solution of the electromagnetic wave equation for a moderately inhomogeneous linearly absorbing medium [28]. In the laser ionization problem of a solid and subsequently expanding target, not only severe inhomogeneities but also reflection of the laser light can play an important role. Reflection can be brought about by steep density gradients and/or by an over-dense plasma, i.e. where the plasma frequency exceeds the frequency of the laser. In the presence of strong inhomogeneities the general problem of plasma absorption should be (and was) treated through the numerical solution of the electromagnetic wave equation.

However, in most of the runs we resorted to the use of Eq. 6 for the extreme requirements which would have been imposed on CPU time and computer memory by the wave equation picture. We checked the consequences of this simplification and found that discrepancies between Eq. 6 and the solution of the wave equation become significant only if spatial inhomogeneities are present at the scale of the wavelength.

The role of non-linear absorption is briefly discussed on pp. 71–75 of [26] and in [6], and turned out to be negligible in the case of our interest. Furthermore, we supposed that also other non-linear phenomena, for instance, the ponderomotive force could be neglected.

Ion formation was treated within the framework of the local thermal equilibrium theory (LTE) [29]. This means that we assumed an equilibrium

between electrons, ions and neutrals (i.e. only one temperature was introduced for the three components). Because of this assumption our model is equivalent to a one-component–one-dimensional model (1C–1D). For the ionization equilibrium the Saha–Eggert equation was used:

$$\frac{n_e n_i}{n_n} = \left(\frac{Q_e Q_i}{Q_n} \right) \left(\frac{m_e m_i}{m_e + m_i} \right)^{3/2} \left(\frac{2\pi kT}{h^2} \right)^{3/2} \exp\left(-\frac{U_i}{kT} \right) \tag{11}$$

Here n_n denotes the number density of the neutrals, Q_e, Q_i and Q_n denote the internal partition functions of electrons, ions and neutrals, respectively, h is Planck's constant and U_i is the ionization potential of the neutrals. Our implementation of Eq. 11 was truly local, as the densities and the temperature were position dependent. According to common practice we neglected in this equation the factor containing the partition functions and simplified the reduced mass to m_e.

During each step of the calculation we determined first the absorbed energy resulting partly from normal absorption, partly from plasma absorption. The absorbed energy elevates the temperature of the system and it supports the energy necessary for the ionization. Both contributions appear in the expression for the internal energy per unit mass (see Eq. 4). We allowed the appearance of singly charged ions only, a limitation which reflects a common feature of laser ionization mass spectra in time-of-flight instruments. For the simultaneous calculation of the temperature and of the ionization degree, η, we had to solve a system of non-linear equations containing Eq. 4 and

$$\frac{\eta^2}{1-\eta} = \frac{1}{n_n + n_i} \left(\frac{2\pi m_e kT}{h^2} \right)^{3/2} \exp\left(\frac{-U_i}{kT} \right) \tag{12}$$

To find the roots of these equations we used an interval-halving method.

We also have to devote a brief discussion to the validity of the LTE approach posed above. For this purpose we compare the electron–ion collision times, τ_{ei}, with the time-step of the integration, Δt. The criterion for the validity of the LTE theory now reads as $\Delta t \gg \tau_{ei}$. In other words, this means that because of the very different electronic and ionic masses, the kinetic energy transfer between them is highly ineffective and a great number of collisions is necessary until equilibrium is reached. The situation is similar to that of the electron–neutral equilibrium with the remark that the neutral density, in general, is higher than the ion density; thus, the condition above is generally sufficient also for the neutral–electron equilibrium. Between ions and neutrals the equilibrium is reached in a time interval similar to the ion–neutral collision time, which is a much weaker condition.

During the calculations these conditions were satisfied quite well for the dense region of the expansion. For the dilute region the LTE model is certainly not valid but, fortunately, in this region only a negligible amount of material is present. A more detailed discussion of this topic was given in [6].

RESULTS AND DISCUSSION

In this section we present a survey of the results for a large group of runs which were intended to unveil the importance of a collection of properties relevant for laser ionization processes. The quantities we will discuss in the subsequent paragraphs are the crater depth in the target, the extent of the plasma expansion at the end of the laser shot, the number of ions which were generated in the laser plume, the relative sensitivity factors and the kinetic energy distributions.

First, let us summarize the main assumptions and simplifications we have made. From the 1C–1D model it followed that the condition of quasi-neutrality was also held, i.e. the electron and ion densities were always equal. This restriction also implied that we neglected the effect of the external electrostatic field. It will be shown later that this assumption was always appropriate. The problem of the penetration of an external electrostatic field in a plasma will be discussed in relation to the kinetic energy distribution.

The residual degree of ionization was set uniformly to 10^{-3}. This value accounted for the free electrons present in many solids, as a result of defects and impurities. A more realistic way to describe the early stage of plasma absorption from a solid target would be the modelling of the kinetics of free electron production at the onset of laser solid interaction. This, however, was beyond the scope of the present work.

During the discussion we will distinguish material and laser parameters. The former are the normal absorption coefficient and the ionization potential of particles in the sample. Values of material parameters were grouped with the aim of representing typical classes of materials, as for instance, metal samples, which have low ionization potential (or work function) and high normal absorption coefficient, and transparent and opaque insulators, which in many cases have higher ionization potentials, etc. This grouping makes the comparison with experimental findings easier although it is oversimplified. In what follows, by "laser parameters" we understand the laser power density and wavelength.

The laser power density covered a range from 10^6 to 5×10^9 W cm^{-2}. This range includes the laser desorption phenomena and also those characteristic of laser plasma ionization experiments.

TABLE 1

Symbols, line types and parameters for Figs. 2–5

Symbol	Line type	Laser	Sample	α_0' (cm^{-1})	$I_{\rm p}$ (eV)
◇	Broken	ruby	Metal	10^4	5
	Dotted		Transp. ins.	10	10
	Solid		Opaque ins.	10^4	10
△	Broken	4ωNd–YAG	Metal	10^4	5
	Dotted		Transp. ins.	10	10
	Solid		Opaque ins.	10^4	10
○	Dotted	CO_2	Transp. ins.	10	10
	Solid		Opaque ins.	10^4	10

For the wavelength dependence investigations we used the frequency values of three widely used lasers: the CO_2 laser ($\lambda = 10.6$ μm), the ruby laser ($\lambda = 0.694$ μm) and the frequency-quadrupled Nd–YAG laser ($\lambda = 0.266$ μm). The last is applied in the commercial LAMMA® and LIMA® instruments [30,31]. The pulse durations of the lasers were set to 150, 20, and 10 ns, respectively. These values were used as integration times for Eq. 1, as target heating takes place only while the laser is shining.

For material parameters the following simplifications were made. We have investigated opaque and transparent samples typically with $\alpha_0 = 10^4$ cm^{-1} and $\alpha_0 = 10$ cm^{-1}, respectively, independent of the wavelengths of the lasers. The values of the ionization potentials covered a range from 4 to 12 eV.

The classification of runs discussed in the subsequent subsections is presented in Table 1. The types of symbols distinguish the laser wavelengths, and the line types refer to different categories. These conventions were used consistently in all the relevant figures.

In the realization of the Godunov scheme, we applied the adaptive grid method, which provided detailed profiles at every stage of the vigorous expansion process. The adaptation of an expanding reference frame containing 100 spatial mesh points was described in [6] in more detail. The calculations were carried out at the University of Antwerp on a VAX 11/780 computer. Typical CPU times were over 30 min.

Before the detailed discussions we make a few remarks on the general features of the profiles at the end of the laser pulse. An example is shown in Fig. 1. It consists of five profiles: velocity, temperature, neutral and ion density (shown in the same plot), and the laser light intensity. The position of the initial solid–vacuum boundary is marked by a vertical bar.

The main characteristic of the velocity profile is the monotonic rising part. For unperturbed expansion, i.e. in the absence of heating, it has been
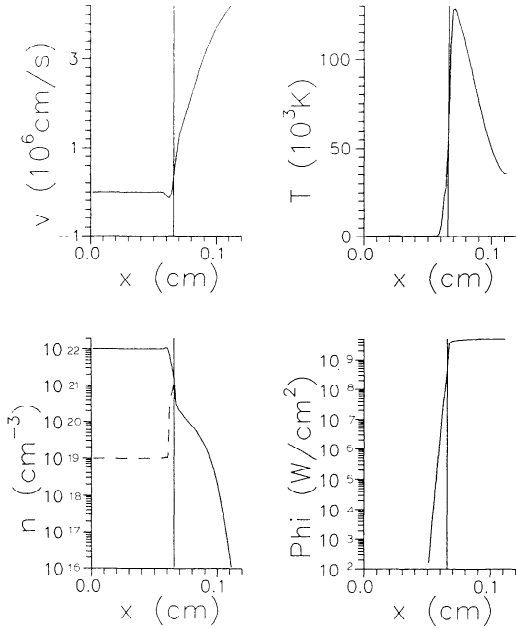
Fig. 1. Sample output of the hydrodynamic code at the end of a 10 ns laser shot. The sample was an opaque insulator of $m = 24$ u. Laser power density was 5×10^9 W cm^{-2}, the wavelength was that of the 4ω. Nd–YAG laser. Vertical bar marks the original position of the solid–vacuum interface. In the density profile the solid line corresponds to the neutral density, the dashed line to the ion density.

demonstrated that this rising part is practically linear [17,20]. The broken and curved rising of the velocity instructs us that the laser-driven expansion cannot be replaced by an approximation in which we let a previously heated system expand adiabatically. The maximal value of the plasma velocity is about 4×10^6 cm s^{-1} at 10^9 W cm^{-2} laser intensity. This corresponds to approximately 200 eV peak kinetic energy for $m = 24$ u particles.

The temperature profile exhibits a sharp maximum in front of the target, rising almost linearly to about 10^5 K (close to 11 eV). The pronounced difference between the kinetic and internal energies justifies the application of hydrodynamics. It is also worth mentioning that our detailed description of plasma expansion provides significantly higher temperatures than earlier LTE calculations did where no spatial distribution of thermodynamic variables was considered [32]. Introduction of heat conductivity into the scheme had no noticeable effect on the temperature distribution.

Inspecting the density profiles we observe that in the case of opaque targets, even at 10^9 W cm^{-2} intensity, complete ionization prevails throughout the whole plasma cloud. Closer investigation of the density and

temperature profiles reveals the existence of two well-known hydrodynamic phenomena: a compression wave toward the interior of the target, and a shock wave in the plasma phase leaving the target. The former is responsible for the splashing of molten material from the crater, and the latter causes the appearance of energetic ions.

The most characteristic feature of the light intensity profile is the extremely sharp fall in the plasma region. Because of the high absorptivity of the plasma, practically no laser light reaches the target surface any longer.

Crater depth

Calculations and measurements of crater depths stemming from laser damage have been rarely reported in the literature [33,34]. Although the crater formation mechanism and hole drilling which take place in laser–target interaction have also a theoretical footing [35], the authors have not found any example of crater depth calculations.

To find the bottom of the crater, we investigated temperature and velocity profiles. To produce noticeable damage in the solid, the temperature had to exceed a certain temperature, which we arbitrarily set equal to the boiling point of the sample. In addition, the velocity had to change sign in the target, as hot material leaves the bulk whereas the compressed solid moves toward the solid phase. Consequently, the zero crossing of the velocity curve provides a readily identifiable point for the determination of the crater depth.

The calculated values, in certain respect, reflect important features confirmed by experiment (see Fig. 2). Damage thresholds, for example, for transparent insulators (ca. 10^9 W cm^{-2}) were higher than those for metals or for opaque insulators (ca. 10^7 W cm^{-2}), in accordance with the measurements of Fürstenau [36]. Furthermore, above the damage threshold, increasing power density always led to deeper craters.
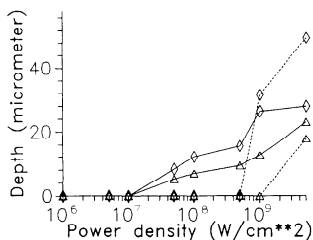
Fig. 2. Crater depths as a function of laser power density at the end of the laser pulse. Lasers are distinguished by different symbols, and targets by different line types (see Table 1).

Because of simplifications of the model (absence of cohesive forces in the solid and omission of several dissipative terms) and the poor resolution of the final profiles, calculated crater depths consistently and significantly exceeded the measured values. However, a systematic investigation of different targets exhibited strong correlation with the data presented in [33].

Cloud extension

As can be seen from Fig. 1, upon laser–solid interaction an important fraction of the laser energy is converted into hydrodynamic flow. For this reason we have been looking for a quantity which is easy to determine and, at the same time, characterizes well the significance of hydrodynamic phenomena. The extension of the expanding cloud seems to be a suitable choice. It can offer some valuable information for experimenters as well.

Cloud extensions were determined from the density profiles by localizing the point where the density decays to the vacuum value. Results are shown in Fig. 3, using the conventions compiled in Table 1.

Before embarking on the discussion of Fig. 3, it is appropriate here to investigate the frequency dependence of the plasma absorption coefficient. This relationship is the key to several phenomena of the subsequent figures.

It was mentioned earlier that the plasma absorption coefficient has a sharp maximum in the vicinity of the plasma frequency. This quantity is determined by the free electron density. At the critical electron density the plasma frequency is equal to the frequency of the laser. This critical density is 9.9×10^{19} cm^{-3} for the CO_2 laser, 2.3×10^{21} cm^{-3} for the ruby laser and 1.5×10^{22} cm^{-3} for the 4ωNd–YAG laser.

As the residual electron density in the solid was 10^{19} cm^{-3}, we can see that it is close to the critical density for the CO_2 laser. An increase in the electron density soon leads to a dramatic increase in the absorption coefficient. This sudden change (and all its consequences) are most pronounced for the CO_2 laser. To reach the critical density for the ruby laser we need a
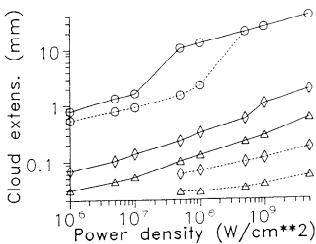

Fig. 3. Cloud extension versus laser power density. Meaning of symbols and line types is specified in Table 1. The mass of the ions was 24 u.

system which in itself is quite extreme (hot and dense plasma), so that the appearance of the resonant-like plasma absorption and its consequences will not be as articulate as in the case of the CO_2 laser. For the 4ωNd–YAG laser, the critical, density could not be reached for this particular solid.

In Fig. 3, because of the similarity in the behaviour of metal targets and opaque insulators we show only six curves. This similarity indicates that the ionization potential plays only a secondary role in hydrodynamic effects.

The investigation of the wavelength dependence demonstrates well the phenomenon to which we referred above. Cloud extensions are highest for the CO_2 laser, and the appearance of the resonant-like plasma absorption is observable at the steep rises of the respective curves. For the ruby laser, we see the characteristic rise for the opaque sample, but it is entirely absent from the remaining curves.

To obtain an "abstract" wavelength dependence we had to compare the cloud extensions for the same pulse-length. A comparison after 10 ns integration time showed the curves closer together, but their position relative to each other has not changed. As the cloud extension is closely related to the temperature of the system, we can say that the CO_2 laser is the most effective for plasma heating under the conditions of laser ionization mass spectrometry. This finding is in accordance with other calculations [37].

An interesting feature of the laser ionization experiments can be discerned from the two curves corresponding to the CO_2 laser. At lower intensities opaque and transparent targets behave differently, whereas at higher intensities the corresponding curves run together. We generalized this observation in the following way: in the low power density domain it is primarily the target parameters which determine the characteristics of the laser ionization processes, whereas in the high power density domain the laser frequency dominates. We have made several checks and found that at very high laser intensity (ca. 10^{11} W cm^{-2}) the cloud extension is a function of the laser wavelength only.

Although experimental determination of cloud extensions has not been carried out yet, there are measurements which provide a basis to estimate them (see, for instance, Chen and Yeung [38]). To illustrate this point, we studied the relationship between the average expansion velocity (which is the cloud extension divided by the pulse length) and the laser power. We found a general power law connecting the average velocity, $\langle v \rangle$, to the light intensity

$$\langle v \rangle \propto I^{\beta}, \qquad (\beta = 0.2 \ldots 0.5) \tag{13}$$

in the region above the damage threshold. It is encouraging that for opaque samples we recover exponents close to the experimental values of Gregg and Thomas [39].

Ion yield

If we integrate the ion density profiles from the crater depth to the cloud extension, we obtain the total number of ions generated by the laser. Results are compiled in Fig. 4.

The two representations in Fig. 4 serve different purposes. Figure 4(a) shows the total number of ions generated, whereas in Fig. 4(b) we normalize these data to the number of photons in the laser shot.

In Fig. 4(a) ion yields are given for a laser beam of 1 cm^2 cross-section. This means that ion yields have to be scaled down by the actual spot size. Taking into account typical spot sizes (10^{-6}–10^{-4} cm^2), ion yield values in Fig. 4(a) are in agreement with experimental results listed in [40].

The presence of a threshold in the ion yield is clearly exhibited in both Figs.4(a) and 4(b). Below the threshold we found ions that originated from the residual ionization of the solid. This indicates desorption of the ions which were already present in the solid phase or on the surface. On exceeding the threshold power density, thermal ionization becomes increasingly dominant until we attain a maximum in the efficiency (see Fig. 4b), which coincides with the appearance of complete ionization in the plasma cloud. A more detailed discussion of the threshold power densities, based on a simpler model, is presented in ref. 41.

As we have mentioned earlier, a significant difference between low- and high-intensity regions can be identified. In Fig. 4(b) this distinction is obvious immediately. At 5×10^7 W cm^{-2} we notice that the normal absorption coefficient and ionization potential of the material are the important parameters: there is no difference between the ion yields produced by the ruby and the 4ωNd–YAG lasers (the CO$_2$ laser has different
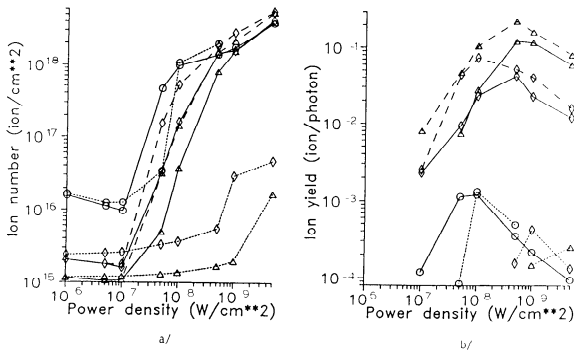

Fig. 4. Total number of ions or ion yield (a) and ion yield normalized to the number of photons (b) versus laser power density. Meaning of symbols and line types is specified in Table 1. The mass of the ion was 24 u.

behaviour, see below). However, we can observe strong differences among different materials. On increasing the power density, the ionization potential clearly loses its significance and the laser frequency gradually gains in importance. We also met this behaviour in the cloud extension subsection.

Comparing Fig. 4(b) with Fig. 3, we find that efficient plasma heating is not a synonym of effective ion production. Whereas the CO_2 laser gives rise to the largest cloud extensions and temperatures, its ionizing capability is surprisingly low. This can be rationalized by the following explanation.

During the absorption the solid–vacuum interface is heated most intensively. In this region the density of neutrals, which is the source of ions, increases from the vacuum toward the bulk phase. In the interface region the ionization degree reaches unity rapidly and a shielding plasma layer is formed in front of the bulk phase. Ion density in this layer amounts to 10^{18}–10^{20} cm^{-3} (see Fig. 1). At this ion density the plasma absorption coefficient is highest for the CO_2 laser, so not only the heating but also the shielding is more effective in this case. On the other hand, in the case of the ruby laser a large fraction of the laser energy can be absorbed in the bulk and a larger fraction of energy contributes to ion production.

Transparent samples are difficult to ionize in the laser intensity domain investigated, with the exception of the CO_2 laser. The sharp rise in ion yield at 5×10^7 W cm^{-2} has the same origin as the sudden change in the slope of the cloud extension curve. We can attribute both phenomena to the early appearance of resonant-like plasma absorption.

Relative sensitivity factors (RSFs)

Our model is also capable of providing RSF values which play an important role in the mass spectrometric analysis of inorganic materials.

According to the simplifications made in Eq. 10, the ionization potential has remained the only material parameter in the expression for the ionization equilibrium. Thus, by plotting the relative ion yields against the ionization potential we obtain estimates for RSF values.

Beusen et al. [42] and Ramendik et al. [43] have developed descriptions for the RSF's as a function of ionization energies. Their theories successfully reproduced a wide range of experimental results; however, they both had two adjustable parameters for curve fitting. In the present model, RSF values were generated without any fitting parameter.

Calculated and measured relative sensitivity factors as a function of the ionization potential of the different elements are compared in Fig. 5. The calculated relative sensitivity curve is quite close to the least-squares fit of the high power density measurements [44]. We can conclude again at high laser intensities material parameters lose their significance. Conzemius and
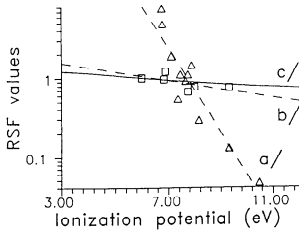
Fig. 5. Relative sensitivity factors versus ionization potential. Dashed lines are least-squares fits to the experimental points. (a) Conzemius and Svec [45] measured steel targets at 2×10^9 W cm^{-2} power density. (b) Bykovskii et al. [44]: Sn targets at 7×10^9 W cm^{-2}. (c) Present theory at 5×10^9 W cm^{-2} power delivered by a 4ωNd–YAG laser on an opaque target.

Svec provided values for lower irradiance where the relative sensitivity varies more with the ionization potential and other material parameters [45]. Lowering the power density in our model by an order to magnitude also resulted in a steeper curve but its slope still did not reach that of line (a) in Fig. 5.

Ion kinetic energy distribution

The kinetic energy distribution of laser-generated ions is poorly understood in spite of some theoretical efforts [5].

Unfortunately, LTE theory using relative intensities of different ions [46] cannot account for the large kinetic energy spread recorded in experiments [47]. In fact, it is surprising that even in mild desorption experiments large organic molecular ions acquire kinetic energies in the electronvolt range (1 eV corresponds to 1.1×10^4 K), without substantial fragmentation. However, by using the hydrodynamic model, we can derive kinetic energy distributions directly from the velocity profiles. In this way, we can account for the coherent motion of particles induced by hydrodynamic forces.

In Fig. 6, we compare measured and calculated ion kinetic energy distributions at low laser power density. The 150 ns pulse from a CO_2 laser was focused on a saccharose–NaCl sample, which yielded—among others—Na$^+$ ions [5]. Fig. 6(a), (ii) shows the deconvoluted experimental kinetic energy spectrum of Na$^+$ ions. Our calculations were carried out with the closest known set of material parameters ($\alpha_0 = 1$ cm^{-1}; $I_p = 8.8$ eV) and provided a distribution displayed in Fig. 6(b). Remarkably enough, the theoretical curve estimates the range of the observable kinetic energies properly.

In Fig. 7(a), curve (i) represents the energy spectrum of Ta$^+$ ions generated by an Nd–YAG laser at elevated power density (2.5×10^{10} W cm^{-2}). Although the absorption coefficient of the Ta sample at the given wave-
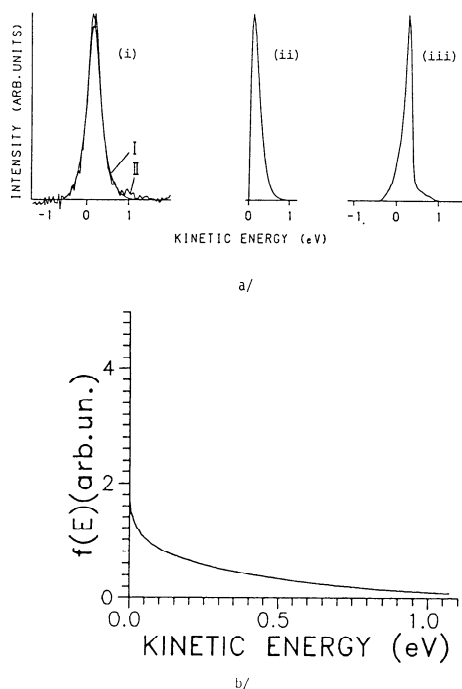
Fig. 6. Measured (a) and calculated (b) ion kinetic energy distributions in case of low laser power density. Measured curves are from Van Der Peyl et al. [5], who studied Na^+ emission from an organic sample. (i) Measured distribution, (ii) deconvoluted kinetic energy distribution, (iii) transmission function of the apparatus. The calculated curve was determined at the same laser intensity for an opaque insulator. A 150 ns shot was delivered by a CO_2 laser.

length was not accurately known we used $\alpha_0 = 10^5$ cm^{-1} as an estimate, on the basis of values determined for other metals.

Figure 7(b) shows the calculated kinetic energy distribution for Ta^+ ions. When comparing Figs. 7(a) and 7(b) it is apparent that the present calculation underestimates the ion kinetic energies in the high power density case; it appears, nevertheless, that the hydrodynamic mechanism can account for a considerable part of it.

Here we mention that the final kinetic energy distribution slightly differs from that shown in Figs. 6 and 7. The expansion continues after the laser heating has ceased, until the surface of the target solidifies again. This additional flow will result in a slight change of the distribution.

A very important point related to the kinetic energy distribution of ions is the role of the external electrostatic field in mass spectrometers. If the accelerating field is able to penetrate the plasma cloud then ions which were formed at different places within the accelerating region are accelerated to
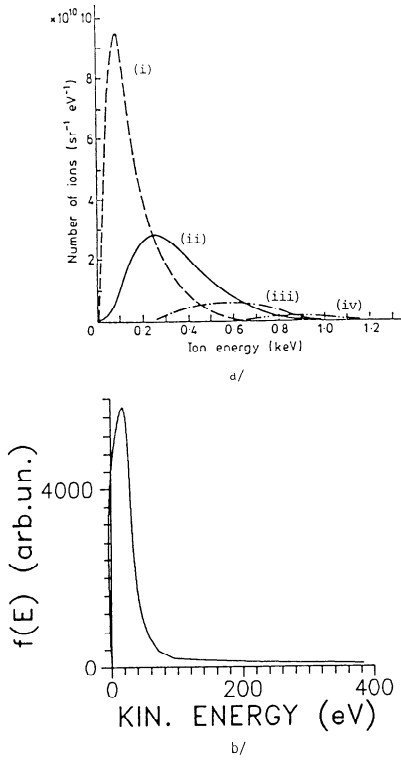
Fig. 7. (a) Experimental (Dinger et al. [47]) and (b) calculated kinetic energy distributions for high laser intensity. In the experiments Ta$^+$ (i), Ta^{2+} (ii), Ta^{3+} (iii) and Ta^{4+} (iv) ions were investigated. The Nd–YAG laser delivered a pulse of 2.5×10^{10} W cm^{-2}. Parameters of the calculations for the Ta$^+$ distribution were the same as those of the experiments.

different kinetic energies. A fraction of the ions become energy deficient, depending on the potential of the spot at which they have formed.

The penetration of an external electrostatic field in a conducting substance is limited. This limit is usually estimated by the characteristic length or Debye-length

$$\lambda_D = \left(\frac{kT}{4\pi e^2 n_e} \right)^{1/2} \tag{14}$$

We have shown in fig. 11 of ref. 6 the Debye-length profiles for different laser intensities and at different stages of the expansion process. It is found that the external field practically cannot penetrate in the plasma cloud during the laser pulse. This justifies our assumptions that the effect of the accelerating field during laser heating can be ignored. With the exception of the outermost layer of the cloud, where only an insignificant amount of material is located, the penetration depth of the accelerating field does not exceed 0.1 μm.

On the other hand, there is much experimental evidence that the kinetic energy spectrum of laser-generated ions can possess an extensive energy-deficient part [8,9,11]. It is probable, however, that other types of ion formation, such as ion/molecule reactions, can be responsible for these energy-deficient ions.

CONCLUSIONS

It is worthwhile at this point to evaluate the achievements and shortcomings of our hydrodynamic model. Despite the numerous simplifications we made to overcome mathematical difficulties, our model was able to account for many important features of laser plasma ionization.

Damage thresholds for different materials were readily recovered, although calculated crater depths exceeded measured values. This weakness, however, can be traced to the absence of cohesive forces and dissipative effects in the model.

Quite convincingly, a clear distinction between heating and ionizing capabilities of different lasers was demonstrated. The absorption coefficient of the sample played a key role in coupling laser energy to the target. The ionization potential had a moderate influence on properties of the generated plasma. The most pronounced differences appeared between the ion yields for metals and opaque insulators.

Other material parameters, such as the heat of evaporation or the energy requirement of fragmentation, are probably important in the low power density domain. Introduction of cohesive forces in the model would result in better understanding of crater formation and of the development of the plasma ball after target resolidification.

To account for the variety of ionic species in laser ionization mass spectra, recombination and other ion/molecule reactions should be included in the model. Local thermal equilibrium would also be violated in this respect, giving rise to a kinetic description of these reactions. Further severe complications would be brought about by the necessity of a multi-component hydrodynamic model.

Our estimation of relative sensitivity factors agreed well with certain high laser intensity measurements and not so well with some others. The general survey of several independent experimental RSF investigations taught us not to have great expectations of establishing a simple $\log(RSF)$–I_p relationship.

The extension of the ion kinetic energy distributions was successfully predicted at low light power densities, but somewhat underestimated at elevated intensities. Nevertheless, according to our knowledge, these calculations represent the first explanation of the existence of high-energy ions originated in laser ionization.

Radial transport of energy probably colours further the picture of ion energetics. Splashing, i.e. radial flow of molten target material, and induced ionization in inhomogeneous targets could be rationalized in a two-dimensional description. On the other hand, two-dimensional hydrodynamics usually leads to numerical problems that are hard to surmount.

The present understanding of low-intensity laser desorption can undoubtedly be refined. Below the onset of thermal ionization in our model the desorbed ions were generated by simply evaporating ions which were already present on the surface. Thus, their abundance was correlated with the arbitrarily set value of the residual degree of ionization. This effect leads to the breakdown of our model near the ion-production threshold. A feasible description of this regime has yet to be provided.

ACKNOWLEDGEMENTS

REFERENCES

1 A.N. Shibanov, in V.S. Letokhov (Ed.), Laser Analytical Spectrochemistry, Adam Hilger, Bristol, 1985, p. 353.
2 F. Hillenkamp, M. Karas and J. Rosmarinowsky, in P.A. Lyon (Ed.), Desorption Mass Spectrometry, American Chemical Society, Washington, 1985, p. 69.
3 G.J.Q. Van Der Peyl, K. Isa, J. Haverkamp and P.G. Kistemaker, Org. Mass Spectrom., 16 (1981) 416.
4 R. Stoll and F.W. Röllgen, Z. Naturforsch., 37A (1982) 9.
5 G.J.Q. Van Der Peyl, W.J. Van Der Zande and P.G. Kistemaker, Int. J. Mass Spectrom. Ion Processes, 62 (1984) 51.
6 A. Vertes, P. Juhasz, M. De Wolf and R. Gijbels, Scanning Microsc., 1988—2 (1988) 1853.
7 D.A. Thompson, Radiat. Eff., 56 (1981) 105.
8 T. Mauney and F. Adams, Int. J. Mass Spectrom. Ion Processes, 59 (1984) 103.
9 E. Michiels, T. Mauney, F. Adams and R. Gijbels, Int. J. Mass Spectrom. Ion Processes, 61 (1984) 231.
10 P. Sigmund, Phys. Rev., 184 (1969) 383.
11 A. Vertes, P. Juhasz, P. Jani and A. Czitrovszky, Int. J. Mass Spectrom. Ion Processes, 83 (1988) 45.

12 P. Mulser, Z. Naturforsch., A, 25 (1970) 282.

13 J.P. Christiansen, D.E.T.F. Ashby and K.V. Roberts, Comput. Phys. Commun., 7 (1974) 271.

14 Comput. Phys. Commun., 48 (1988) (the whole volume is devoted to the hydrodynamic modelling of laser plasmas).

15 S.K. Godunov, Mat. Sborn., 47 (1959) 271 (in Russian)

16 L.D. Landau and E.M. Lifshitz, Theoretical Physics, Vol. 6, Addison–Wesley, Reading, MA, 1959, Chap. 9.

17 A.V. Gurevich, L.V. Pariiskaya and L.P. Pitaevski, Sov. Phys.—JETP, 22 (1966) 449.

18 R.D. Richtmyer and K.W. Morton, Finite Difference Methods for Initial Value Problems, Wiley, New York, 1967, p. 306.

19 J. von Neumann and R.D. Richtmyer, J. Appl. Phys., 21 (1950) 232.

20 C. Sack and H. Schamel, Phys. Rep., 156 (1987) 311.

21 S.K. Godunov, A.V. Zabrodin and G.P. Prokopov, USSR Comput. Math. Math. Phys., 6 (1961) 1020.

22 M. Karas, D. Bachmann and F. Hillenkamp, Anal. Chem., 57 (1985) 2935.

23 M. Karas, D. Bachmann, U. Bahr and F. Hillenkamp, Int. J. Mass Spectrom. Ion Processes, 78 (1987) 53.

24 T.P. Hughes, Plasmas and Laser Light, Adam Hilger, Bristol, 1975, Chap. 1.

25 J. Dawson, P. Kaw and B. Green, Phys. Fluids, 12 (1969) 875.

26 P. Mulser, R. Sigel and S. Witkowski, Phys. Rep., 6 (1973) 187.

27 L. Spitzer, Physics of Fully Ionized Gases, Interscience, London, 1956, p. 65.

28 V.L. Ginzburg, The Propagation of Electromagnetic Waves in Plasmas, Pergamon, Oxford, 1964, Chap. IV.

29 H.W. Drawin, in M. Venugopalan (Ed.), Reactions under Plasma Conditions, Wiley, New York, 1971, p. 53.

30 Cambridge Mass Spectrometry Ltd., Cambridge, UK.

31 Leybold–Heraeus, Cologne, F.R.G.

32 U. Haas, P. Wurster, Fres. Z. Anal. Chem., 308 (1981) 270.

33 I.D. Kovalev, G.A. Maksimov, A.I. Suchkov and N.V. Larin, Int. J. Mass Spectrom. Ion Phys., 27 (1978) 101.

34 M.J. Southon, M.C. Witt, A. Harris, E.R. Wallach and J. Myatt, Vacuum, 34 (1984) 903.

35 M. von Allmen, J. Appl. Phys., 47 (1976) 5460.

36 N. Fürstenau, Fres. Z. Anal. Chem., 308 (1981) 201.

37 D.L. Kwong and D.M. Kim, J. Appl. Phys., 54 (1983) 366.

38 G. Chen and E.S. Yeung, Anal. Chem., 60 (1988) 864.

39 D.W. Gregg and S.J. Thomas, J. Appl. Phys., 37 (1966) 4313.

40 R.J. Conzemius and J.M. Capellen, Int. J. Mass Spectrom. Ion Phys., 34 (1980) 197.

41 A. Vertes, M. De Wolf, P. Juhasz and R. Gijbels, Anal. Chem., 61 (1989) 1029.

42 J.M. Beusen, P. Surkyn, R. Gijbels and F. Adams, Spectrochim. Acta, 38, part B (1983) 843.

43 G.I. Ramendik, B.M. Manzon, D.A. Tyurin, N.E. Benyaev and A.A. Komleva, Talanta, 34 (1987) 61.

44 Yu. A. Bykovskii, T.A. Basova, V.I. Belousov, V.M. Gladskoi, V.V. Gorshkov, V.G. Degtyarev, I.D. Laptev and V.N. Nevolin, Sov. Phys. Tech. Phys., 21 (1976) 761. Data also available in [40].

45 R.J. Conzemius and H.J. Svec, Anal. Chem., 50 (1978) 1854.

46 D.M. Hercules, R.J. Day, K. Balasanmugam and S.K. Visvandaham, Anal. Chem., 54 (1982) 280A.

47 R. Dinger, K. Rohr and H. Weber, J. Phys. D, 13 (1980) 2301.